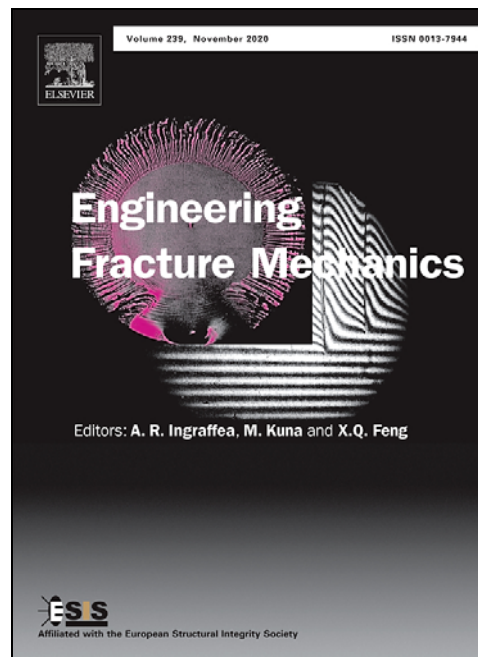


Université de Mons

Faculté Polytechnique – Service de Mécanique Rationnelle, Dynamique et Vibrations

31, Bld Dolez - B-7000 MONS (Belgique)

065/37 42 15 – georges.kouroussis@umons.ac.be



L. Ben Fekih., O. Verlinden, G. Kouroussis, Derivation of a fatigue damage law for an adhesive from in-situ bending tests, *Engineering Fracture Mechanics*, 245, 107587, 2021.



Derivation of a fatigue damage law for an adhesive from in-situ bending tests

Lassaad Ben Fekih^{*}, Olivier Verlinden, Georges Kouroussis

University of Mons, Department of Theoretical Mechanics, Dynamics and Vibrations, Place du Parc 20, 7000 Mons, Belgium

ARTICLE INFO

Keywords:

Space electronics
Ablestik 8-2 adhesive
In-situ bending tests
Cohesive elements
Fatigue damage

ABSTRACT

The adhesives used for the attachment of electronic components to space boards should withstand harsh vibrations of the space launch, which requires their characterization in fatigue. The present study investigates Ablestik 8-2 epoxy adhesive within this context. Novel adhesive test assemblies were devised, which consist of a rigid ceramic component bonded to a resonant flexible epoxy-fibreglass (E-glass) support. Cantilever and square E-glass supports produced uniaxial and biaxial bending, respectively. The in-situ fatigue tests, conducted on batches of uniaxial/biaxial bending adhesive assemblies, led to distinct data sets of maximum support deflection versus the number of cycles to crack initiation/total failure. The derivation of an intrinsic fatigue damage law of the adhesive relied on the substitution of deflection by the maximum principal strain of each adhesive point while keeping the Basquin's form. In so doing, the adhesive strain was computed from finite element models of test assemblies built and simulated under Abaqus. The adhesive layer was meshed by cohesive elements created through a Fortran user-element subroutine coupled to Abaqus. The subroutine incorporated an already validated static damage together with the strain-based fatigue damage law sought. The retained Basquin's fatigue damage law has undergone calibration against uniaxial bending test data and validation by biaxial bending test data.

1. Introduction

The space equipment undergoes harsh vibrations during the launch phase, including quasi-static, harmonic, transient, and random accelerations stemming from thrust, pumps and motors, pogo effect, aerodynamic forces, and engine oscillations [1]. NASA report [2] claims that space launch vibrations are responsible for 45% of spacecraft malfunctions and that electronic malfunctions cause 50% of missions' failure. In this context, structural adhesives are substantial to consolidate the solder joints of electronic components embedded in printed circuit boards (PCBs). The dynamic loads entail PCB curvature so as to load the adhesive joints in fatigue [3]. Under such circumstances, the fatigue properties of adhesives are necessary for the design of reliable electronics. In contrast, datasheets of adhesives rarely include this data. The present work aims at identifying the fatigue properties of Ablestik 8-2, a non-conductive unfilled epoxy adhesive produced by Henkel. A specific interest is directed to the application of this adhesive to bond ceramic electronic components in power distribution and control units, the part of a satellite that ensures power conditioning from solar arrays to batteries. The emulation of this application relies on test adhesive assemblies made of a rigid ceramic component adhesively bonded to a flexible epoxy fibreglass (E-glass) support. To the authors' best knowledge, no prior research has investigated this adhesive arrangement. According to [4], the materials deployed in space applications are restrained to work in their elastic range. This requirement applies to the substrates involved in this work.

^{*} Corresponding author.

E-mail address: lassaad.benfekih@umons.ac.be (L. Ben Fekih).

Nomenclature**Subscripts**

a	Adhesive material
c	Critical
d	Diagonal component, dissipation
l	Fibre lengthwise
m	Mixed-mode conditions
n, s, t	Normal, scissoring shear, transverse shear
p	Principal direction
S	Equivalent shear (transverse+scissoring)
T	Total

Superscripts

$0, f$	Onset, total failure
e	Effective
th	Threshold

Greek letters

β	Mixed-mode ratio
Δ_i, Δ	Component of, equivalent displacement jump
ϵ	Strain quantity
λ	Fatigue parameter
ν	Poisson's ratio
ϕ	Phase lag

Roman letters

(x, y, z)	Cartesian coordinates
a	Crack length
a_b, a_c	Base, response accelerations
C, b	Fatigue parameters
D_f, D_s, D_t	Fatigue, static, total damage variables
E, G	Young's, shear moduli
e_l	Element edge length
F	Excitation/load force
f	Excitation frequency
G	Strain energy release rate
h_a	Adhesive thickness
K	Adhesive stiffness
N	Number of fatigue cycles
N_i, N_f	Number of cycles to specimen onset, total failure
t	Time
T_i, T	Component of, equivalent cohesive stress
Z	Maximum deflection

Acronyms

CZ	Cohesive zone
DCB	Double cantilever beam
FM	Fracture mechanics
HSC	High-speed camera
MMB	Mixed mode bending
PCB	Printed circuit board
SG	Strain gage

From an experimental point of view, the literature encompasses various conventional fatigue test adhesive assemblies, e.g., shear lap specimens [5,6], butt assemblies [7], double cantilever beams (DCB)s [8], and mixed-mode bending (MMB) specimens [9]. Only a few studies dealt with the high cycle fatigue of adhesives used in electronics, which subjected to cyclic bending of the electronic board. Walter et al. [10] investigated the fatigue of polyimide thin film stacks and established thresholds of strain energy release rate, G , to the onset of epoxy adhesive delamination. Fatigue tests relied on a four-point bending set-up, which according to the authors, ensures steady-state crack growth but suffers from insufficient strain energy for the advancement of interface crack. Guzek et al. [11] studied the fatigue crack propagation on DCBs made of nickel or copper bonded with silica-filled polymers. They found that the crack growth rate has a power-law dependence on ΔG , the cyclic variation of G . The resistance to fatigue crack propagation tends to increase with as-plated and blasted substrate surfaces. Jung and Paik [12] investigated the effect of the adhesion strength for a low modulus non-conductive epoxy film at the cyclic bending of copper/film/fabric laminates. These studies assessed the importance of chemical/surface treatments for the enhancement of the fatigue lifetime of adhesive joints but were not involved in the characterization of the adhesive material. Besides, note that most existing test set-ups contained an initial crack tip. The latter cannot, unfortunately, emulate the initiation of crack on actual assemblies, not necessarily cracked. Furthermore, the afferent monitoring methods, e.g., acoustic emission recording and scanning electron microscopy with digital image correlation convene better to track static crack front location than a propagating crack. From a numerical point of view, this work aims at settling a suitable fatigue damage model for the tested adhesive; a static damage model has already been validated in Ref. [13]. Fatigue damage models divide into three categories. The first category of models relies on continuum damage mechanics, where a fatigue damage variable alters the stiffness or/and strength of the adhesive. These methods suffer from the non-convergence of stress predictions at singularities, e.g., free edges and corners. The second category of models hinges on fracture mechanics (FM), mostly Paris' law variants expressing the crack growth rate as a function of G . Bak et al. [14] benchmarked on a cylinder model involving normal opening Paris' law variants based on the cyclic variation of G , those developed by Kawashita and Hallett [15], Bak et al. [16], and Pirondi and Moroni [17] together with Turon et al. [18] and Harper and Hallett [19] models based, alternatively, on the total specific work instead of G . Kiefer [20] pertinently compared the computational performance of Paris' law-based models presented in [15,21,22]. Here, Paris' law variants are not sought since their limitation to crack propagation, i.e., omit crack initiation, so their suitability for the simulation of the delamination of layered composite structures. The third category includes cohesive zone (CZ) models, which link the damage rate to the equivalent displacement jump, strain, or cohesive stress in any material point of the adhesive interface. In general terms, the CZ modelling is preferable to the FM approach because it supports the entire fracture process. Unlike continuum mechanics, CZ modelling circumvents stress singularities. In return, it is important to set the size of the cohesive elements properly. In this category, Robinson et al. [23] and Bouvard et al. [24] formulated the fatigue damage rate through three-coefficient mathematical expressions involving variables of the displacement jump and the cohesive stress, respectively. The limitations of the two preceding models consist in their excessive number of parameters, the dependency of the results on the predictive capabilities of these parameters, and the conditions in which they are determined. For instance, Robinson's parameters do not emanate directly from experiments but rather from trial and error fitting of simulated results against experimental ones. Turon et al. [18] pioneered the combination of CZ and FM (Paris' law) models to account for quasi-static and fatigue crack propagations, respectively. In detail, the authors expressed a total (static+fatigue) damage rate as the product of the growth rate of the damaged area and the derivative of the said total damage with respect to the damaged area of a cohesive element. Bak et al. [25] followed a hybrid paradigm along which the static damage variable only applies during the ramping up phase. At the onset of fatigue cycling, the opening displacements and tractions are frozen, and another variable referred to as the energy variable takes over. The authors established a mathematical expression that links the energy damage rate to the growth rate in any material point, which incorporates the slopes of the equivalent displacement jump and local mixed-mode ratio with respect to the crack growth multiplied by rates of interface opening and mode mixity, respectively. In our opinion, the drawback of Bak et al. [25] model relates to the discontinuous switch to 0 of the cohesive stress when total specific work becomes equal to the energy release rate. More recently, Carreras et al. [26] extended the model achieved in Ref. [25] to the simulation in 3D of fatigue-driven delamination of layered structures involving non-negligible fracture process zones and arbitrarily shaped crack fronts. That said, the common advantage of the aforementioned hybrid models is the non-requirement to parameters fitting. Lastly, Khoramishad et al. [27] developed a fatigue model based on the maximum principal strain, ϵ_p , which reads:

$$\frac{dD_f}{dN} = C \left(\epsilon_p - \epsilon_p^{th} \right)^b \quad \text{if } \epsilon_p > \epsilon_p^{th} \quad \text{and} \quad \frac{dD_f}{dN} = 0 \quad \text{elsewhere.} \quad (1)$$

D_f and N designate the fatigue damage variable and the number of fatigue cycles, respectively. C and b are coefficients of the fatigue law. Below the endurance limit, ϵ_p^{th} , no fatigue damage occurs. ϵ_p depends on the adhesive damage and mode mixity, which are variable in general. The fact that Eq. (1) is apparent to a classical Basquin's law makes it preferable in this study.

This work is structured as follows: the second section unveils the experimental set-ups of Ablestik 8–2, the different techniques deployed to detect the initiation of damage in the adhesive, and a summary of results. The third section focuses on the finite element modelling of test assemblies. It also provides details on static and fatigue damage models attributed to adhesive elements. Next, the fourth section covers the derivation of an intrinsic fatigue damage law for the adhesive through a combined experimental-numerical updating procedure. The resulting fatigue damage law is validated in the fifth section before concluding.

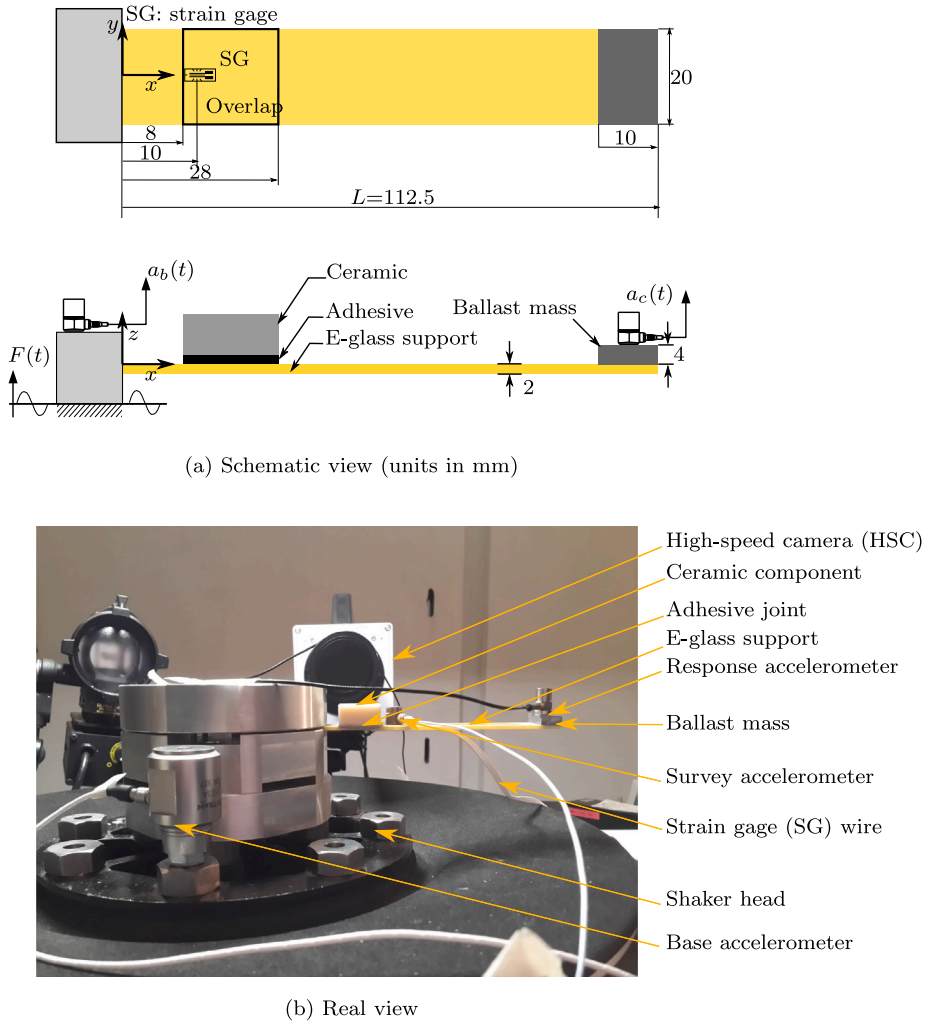


Fig. 1. Fatigue test set-up under uniaxial bending.

2. Experiments

2.1. Resonant fatigue testing of adhesive joints under uniaxial bending

2.1.1. Set-up description

The uniaxial adhesive assembly consists of a ceramic electronic-like component made of pure alumina (99% Al_2O_3) adhesively bonded on a resonant cantilever E-glass laminate of 2 mm thickness.

Ablestik 8–2 adhesive was dispensed with 0.2 mm uniform thickness over the entire overlap area. Calibrated silicon balls guaranteed the thickness uniformity of the adhesive joint. The adhesive was cured at 75 °C for 4 h, which procured its optimal mechanical performance. Finding the appropriate location of the component on the E-glass cantilever that avoids premature or too slow adhesive failure necessitated several attempts. Fig. 1a shows the adopted geometry. The uniaxial adhesive assembly embeds a strain gage (SG) located at 2 mm from the most loaded adhesive bond-line. The latter measures the support backplane longitudinal strain, ϵ_l in the hope of detecting primarily the initiation of the failure and secondarily its propagation. Fig. 1b illustrates the actual set-up comprising a uniaxial bending assembly, a shaker, and a high-speed camera (HSC) deployed in front of the adhesive critical region to monitor crack initiation and propagation. As shown in Fig. 1b, the steel mass bonded at the free end of the E-glass cantilever permits to reach the requested deflection with minimum $F(t)$, excitation force of the shaker. A control routine ensured the excitation of the specimen at a frequency, f , adjusted continuously to its exact fundamental frequency and concurrently maintained the maximum E-glass support deflection, Z , fixed to a user-specified level. Inputs of the control routine consist of signals of the excitation base and response accelerometers, denoted by a_b and a_c , respectively. The base accelerometer is glued on the moving armature of the shaker, while the response accelerometer is affixed on the support free end. The control routine outputs time histories of Z , f , ϕ the phase lag between a_b and a_c accelerations.

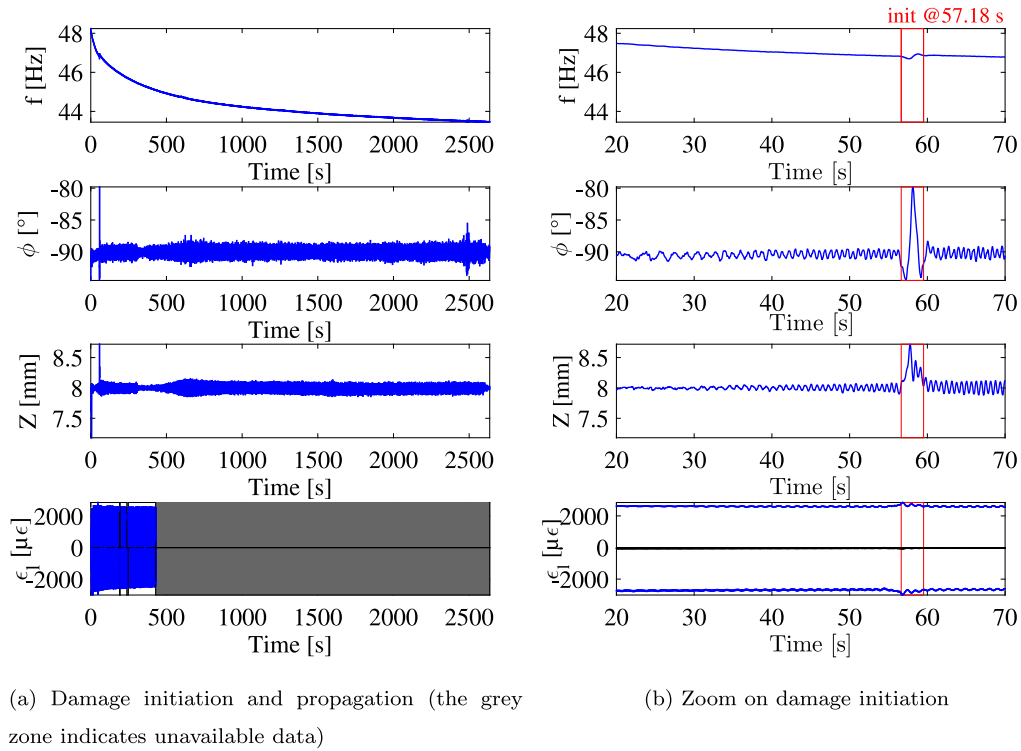


Fig. 2. Monitoring of damage initiation and propagation on a uniaxial bending assembly tested at $Z = 8$ mm.

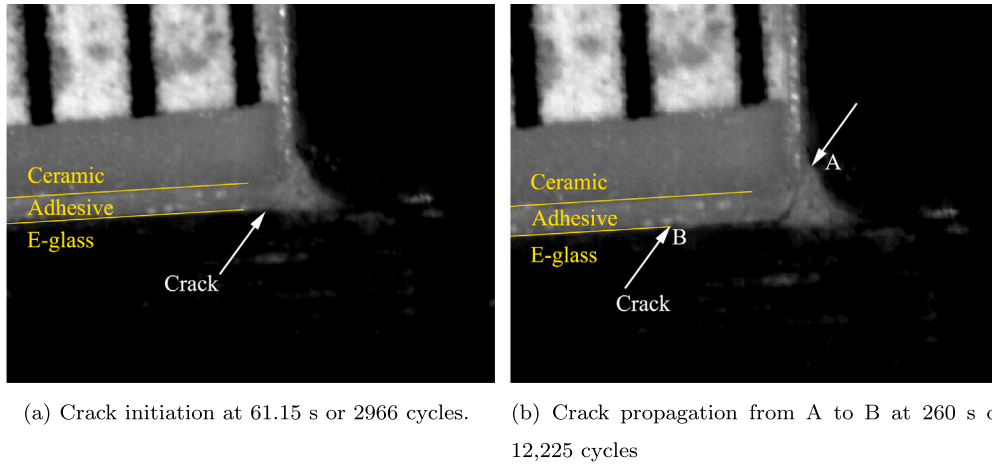


Fig. 3. Detection of the adhesive crack initiation and propagation using a HSC during the fatigue test of Ablestik 8-2 in uniaxial bending at $Z = 8$ mm.

2.1.2. Analysis of results

Fatigue tests were carried out for eight uniaxial assemblies at different deflections Z within 15 mm where no crack occurred on this arrangement under static testing [13]. The analysis of test data relies on three vibratory indicators, viz., f , ϕ and Z , as well as ϵ_l , tracked over the whole test duration. Fig. 2a shows clear decrease of f and ϵ_l , indicative of a progressive interface opening. In turn, the evolution of ϕ is characteristic of a resonance. Regarding the failure initiation, perturbations are discernible from ϕ and Z evolutions as magnified on Fig. 2b reporting test data in [20–70]s range of specimen ID 4 tested at $Z = 8$ mm. If the phase exhibited the highest sensitivity to the initiation of failure, the detectability remains guaranteed from Z and less evident from f . With $Z = 8$ mm, a first crack appeared at 61.15 s, or equivalently after 2966 cycles, against 57.18 s obtained by ϕ for a meniscus checked safe before fatiguing (Fig. 3a). Fig. 3b shows that the crack propagated from the interface between the adhesive joint and the E-glass support.

Table 1
Cycles to the initiation of failure of Ablestik 8-2 adhesive in uniaxial bending.

ID.	Z [mm]	$N_i(\phi)$	$N_i(HSC)$
1	6	14,173	–
2	7.25	5514	–
3	8	3061	3357
4	8	3156	3324
5	8	2754	2966
6	10	1647	–
7	12.5	1023	–
8	15	689	–

Table 2
Cycles to failure of Ablestik 8-2 adhesive under biaxial bending.

ID.	Z [mm]	N_f [Cycles]
1	1.5	650,367
2	2.0	34,877
3	2.0	25,512
4	2.0	33,941
5	2.5	13,040
6	2.5	14,036
7	2.5	12,575
8	3	2336
9	3	2345
10	3	2265
11	3.5	277

Table 1 reports $N_i(\phi)$ and $N_i(HSC)$, namely the number of cycles to failure initiation issuing from ϕ and HSC detections, in terms of applied deflections at the free end of the support. Obtaining an identical initiation for three specimens tested at the same level ($Z = 8$ mm) provides confidence in the vibratory indicators, notably the phase and the relative displacement. Yet, the detection of adhesive damage onset is still a challenging subject for the scientific community. It is noteworthy to mention that fatigue tests were stopped when the frequency curve flattened. At this event, the total failure of tested specimens was not reached. Note that under static loading, almost 3/4 of the adhesive joint area was failed along the longitudinal axis as reported in Ref. [13].

2.2. Resonant fatigue testing of adhesive joints under biaxial bending

2.2.1. Set-up description

The biaxial bending assembly consists of a square E-glass support pinned from its corners with a ceramic component adhesively bonded in its centre. A ballast mass is attached to the ceramic component to attain the support deflections required by the fatigue testing campaign (Fig. 4). Reducing the area of the ballast mass permitted to avoid as much as possible mass unbalance so that to enhance test repeatability. SGs were placed along diagonals of the E-glass support from its backplane 5 mm distant from the component's corners. Their role consists in the survey the adhesive damage and the detection of the corner that will fail first (Fig. 5). Authors recognize that the placement of SGs inside the overlap region could have been more appropriate.

2.2.2. Analysis of results

All tested specimens exhibited a slight drift of the resonance frequency over fatigue cycling. As an example, Fig. 6 reports monitoring of damage for specimen ID6. Unlike uniaxial assemblies, it was not possible to detect neither sudden peaks nor crack propagation. Only the negative peaks of ϵ_d , the E-glass support diagonal backplane strain, fell from -790 to $-664 \mu\epsilon$. These negative strain values are indicative of upward bending of the E-glass support (its backside in compression). In the meanwhile, positive strain values remained unaltered since borders of the component come against the support, which hinders the monitoring of adhesive damage. Two scenarios can explain these results: either the initiation of the crack was reached quickly followed by slow crack propagation until total failure, or (2) the fatigue lifetime was mainly governed by crack initiation so that crack propagation occurred very rapidly at the end of the test. The second scenario usually concerns tough adhesives. Observed strain variations can arise from heating or poor bonding of the SG, and not necessarily from adhesive damage. The assimilation of strain variations to stiffness loss requires more evidence by deploying suitably instrumented specimens.

Presently, Table 2 summarizes test results in terms of cycles to failure, N_f , versus Z . Overall, results are consistent as N_f decreases with increasing Z . The dispersion of N_f values is quite moderate. In addition, values issuing from the same applied deflection constitute separated groups, which is very promising.

Fig. 7 illustrates the fractography of specimens ID1, ID3, and ID9. Although being tested at different Z levels, the three detached faces of ceramic components are visually identical. The adhesive remains mainly on the ceramic component, while a very thin

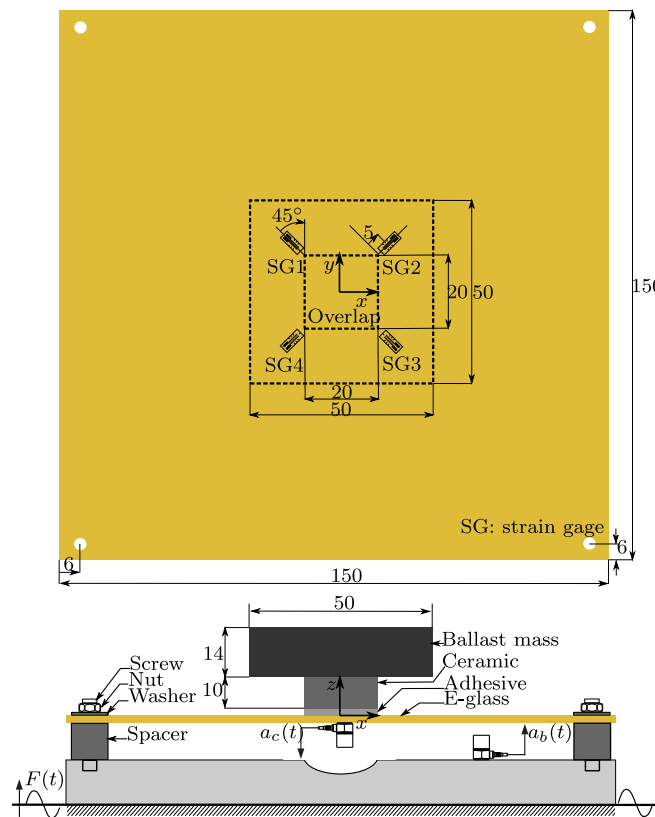


Fig. 4. Fatigue test adhesive assembly under biaxial bending.

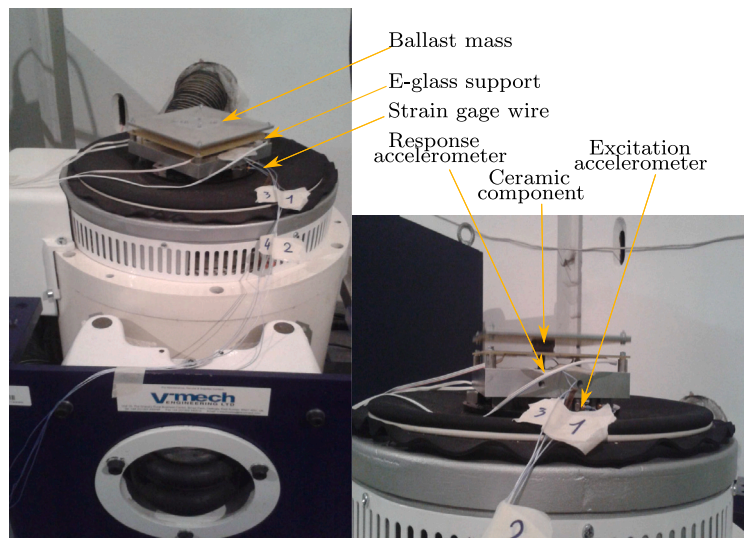


Fig. 5. Fatigue test set-up under biaxial bending.

adhesive film sticks to the E-glass support. This finding is undeniably verified from measures of a profilometer sliding, at the start, on a bare ceramic component, then continuing its path over 15 mm along the centreline of a detached ceramic component. Thickness profiles reported in Fig. 7 indicate that almost 90% of the adhesive thickness remains on the ceramic component. These results corroborate the quasi-interfacial nature of crack propagation on biaxial assemblies.

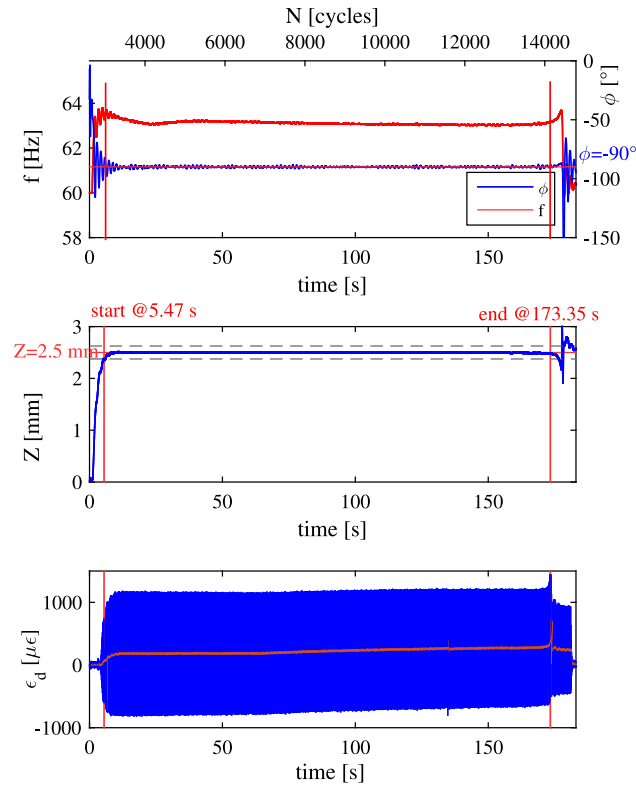


Fig. 6. Monitoring of damage initiation and propagation on a biaxial bending assembly at $Z = 2.5$ mm.

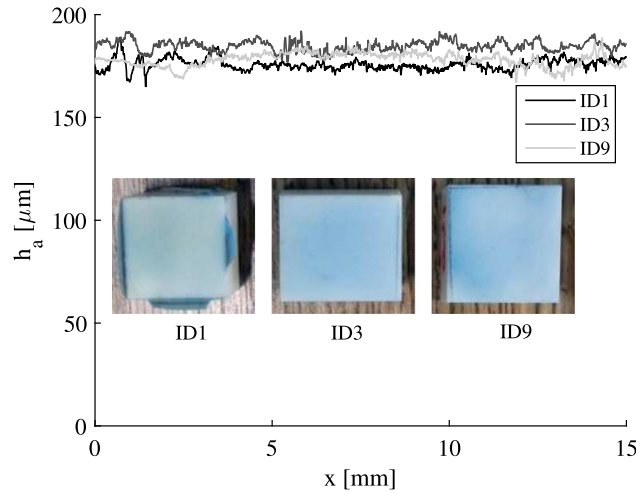


Fig. 7. Measurement of the remaining adhesive thickness ceramic components detached from biaxial assemblies.

2.3. Determination of deflection-based Basquin's fatigue laws

To summarize, eight uniaxial and eleven biaxial test assemblies led to determine the number of cycles to failure initiation N_i , and total failure N_f , respectively. Fig. 8 sketches out N_i and N_f evolutions as function of Z levels in a log-log scale. If the standard of fatigue testing requires a battery of at least 20 specimens, proceeding with fewer specimens is deemed acceptable as long as test data are meaningful. Indeed, uniaxial and biaxial test data were fitted by distinct Basquin's log-linear laws, expressed by

$$N_f(Z)^b = C \quad (2)$$

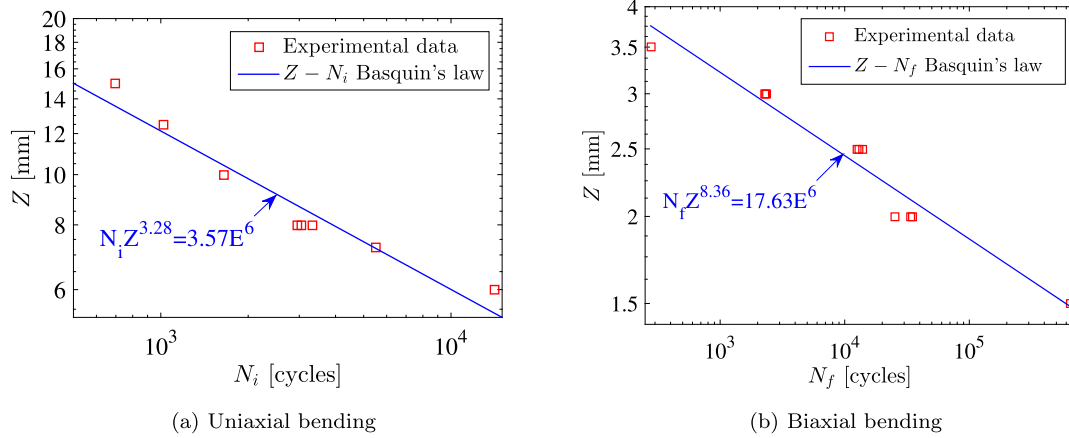


Fig. 8. Basquin's laws fitting fatigue test data under uniaxial and biaxial bending.

where b and C represent Basquin's parameters [28]. R-squared statistics deemed indicators of goodness of fit are worth 93.16% and 94.24% applied to uniaxial and biaxial data, respectively.

The slope of Basquin's curve under uniaxial bending is higher compared to biaxial bending, which is imputable to differences in N_i and N_f numbers of cycles to the initiation and total failure, respectively. The next section will deal with the numerical modelling of the adhesive joint to substitute Z with a local adhesive strain metric as an effort to synthesize an intrinsic Basquin's law for Ablestik 8–2.

3. Finite element modelling of test adhesive assemblies

3.1. Static damage model

The adhesive behaviour is described by a bilinear cohesive law, which reads:

$$T_i = (1 - D_s) K_i \Delta_j - D_s K_i \delta_{ni} \langle -\Delta_n \rangle \quad i, j = n, s, t \quad (3)$$

T_i , Δ_i , K_i designate the i th components of cohesive traction, relative displacement, and stiffness, respectively. (n, s, t) refer to the normal, scissoring shear and transverse shear opening modes. $\langle \cdot \rangle$ is referred to as the MacAuley bracket defined by $\langle \cdot \rangle = \max(0, \cdot)$. Appendix A provides more insight into the cohesive zone modelling (CZM) approach and reasons behind the choice of the bilinear law. According to Camanho and Davila [29], the static damage variable, denoted by D_s , is defined by

$$D_s = \min \left[1, \frac{\Delta_m^f (R - \Delta_m^0)}{R (\Delta_m^f - \Delta_m^0)} \right] \quad (4)$$

R is defined according to $R = \max(R, \Delta)$ with $\Delta = \sqrt{\langle \Delta_n \rangle^2 + \Delta_s^2 + \Delta_t^2}$. Both uniaxial and biaxial bending load the adhesive under mixed-mode conditions. Δ_m^0 and Δ_m^f refer to the mixed-mode displacement jumps at the onset and total failure, respectively. Δ_m^0 and Δ_m^f substitute for Δ_i^0 and Δ_i^f their counterparts in single-mode with $i = n, s, t$. They depend on the mixed-mode ratio contrary to Δ_i^0 and Δ_i^f , which are immutable. The quadratic nominal stress and power law are the initiation and propagation criteria chosen in this work to establish Δ_m^0 and Δ_m^f , respectively. Δ_m^0 and Δ_m^f expressions are included in Appendix A.

The original static damage expression of Camanho is thermodynamically inconsistent. To remedy this, De Moura et al. [30] proposed to substitute the previous one-step displacement-based implementation of Camanho with an incremental energy-based form expressed by

$$D_s^{(k)} = 1 + \frac{\Delta_m^0}{R^{(k)}} \left(\frac{G_d^{(k)}}{G_{mc}^{(k)}} - 1 \right) \quad (5)$$

where $G_d^{(k)}$ and $G_{mc}^{(k)}$ designate dissipation and toughness energies at the increment (k) , respectively. The development of Eq. (5) is documented in Ref. [30]. The energy terms at increment k read as follows:

$$G_{mc}^{(k)} = \frac{1}{G_T^{(k)}} \left(\frac{G_n^{(k)}}{G_{nc}} + \frac{G_s^{(k)}}{G_{sc}} + \frac{G_t^{(k)}}{G_{tc}} \right) \quad (6)$$

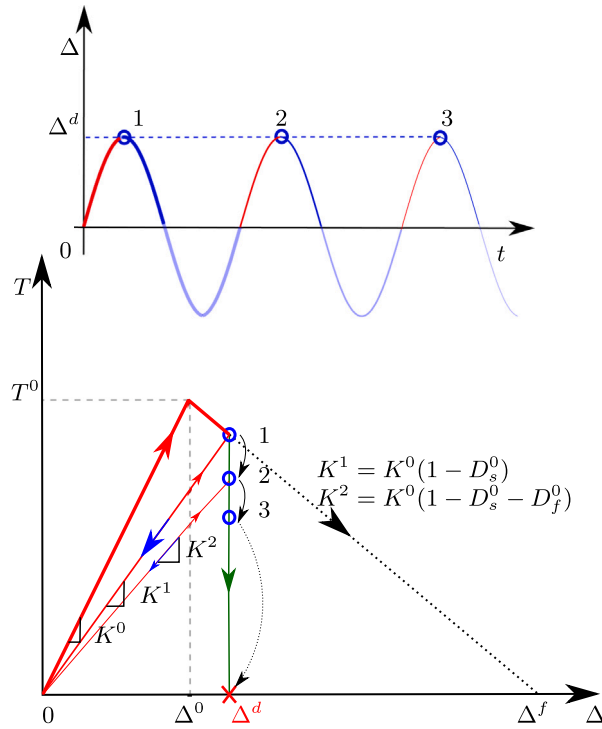


Fig. 9. Non-additive fatigue approach applied to a cohesive element at controlled Δ^d .

$$G_d^{(k)} = G_d^{(k-1)} + \sum_{i \in (n,s,t)} \left(\frac{T_i^{(k-1)} \Delta_i^{(k)} - T_i^{(k)} \Delta_i^{(k-1)}}{2} \right) \quad (7)$$

where $G_T = G_n + G_s + G_f$. The strain energy release rates denoted by G_i are evaluated incrementally following:

$$G_i^{(k)} = G_i^{(k-1)} + \left(\frac{T_i^{(k-1)} + T_i^{(k)}}{2} \right) (\Delta_i^{(k)} - \Delta_i^{(k-1)}) \quad (8)$$

where

$$T_i^{(k)} = (1 - D_s^{(k)}) K_i \Delta_i^{(k)} \quad (9)$$

The damage variable $D_s^{(k)}$ intervenes at the same time as an input of Eq. (9) to compute Eqs. (8) and (6) and as an output of Eq. (5). Its determination requires, thus, an iterative solving method. De Moura et al. [30] told nothing about their iterative algorithm to resolve $D_s^{(k)}$, which led to implementing the secant method owing to its simplicity. Such a method operates at each increment (k) yielding iteratively $D_s^{(k)}$ and $G_{mc}^{(k)}$. De Moura et al. [30] scheme has been implemented into a UEL Fortran user element subroutine, then benchmarked on a standard MMB specimen, as reported in Appendix B.

3.2. Fatigue damage model

The computation of fatigue damage can be separated into additive and non-additive schemes [31]. An additive scheme consists in degrading the adhesive stiffness using a total damage variable $D_t = D_s + D_f$. Following this approach, any cohesive integration point is deemed fully damaged at $D_t = 1$ (Robinson et al. [23]).

A non-additive scheme lies either in D_f or D_s to degrade the adhesive stiffness. The failure takes place whether D_s or D_f becomes equal to 1 [27]. Ghovanlou et al. [32] used D_f to degrade the adhesive stiffness without counting on D_s . Fig. 9 sketches out the concept of non-additive damage under cyclic controlled displacement, Δ^d for an integration point. The static damage applies when Δ exceeds Δ^0 . Fixing Δ^d leads to maintain D_s at D_s^0 , the static damage at the first reached Δ^d . In the meanwhile, D_f is cumulated over cycles. Thereby, the adhesive stiffness decreases gradually following a vertical line. The same evolution is expected under constant fatigue loading afflicted by D_f , only.

Fig. 10 lays out the additive concept illustrated by a cohesive element subjected to controlled applied stress, T^d , over three loading cycles to simulate the change of D_f . D_s is computed at each time increment, k . It differs from zero when T exceeds T^0 , e.g., when T^d is reached. D_s^0 is evaluated from the initial static damage curve, i.e., the line connecting (Δ^0, T^0) to $(\Delta^f, 0)$. The effects of D_s^0 are twofold: (1) loading of the second peak with an interface stiffness worth of $K^0(1 - D_s^0)$ (2) switching Δ from Δ^1 to Δ^2 . By

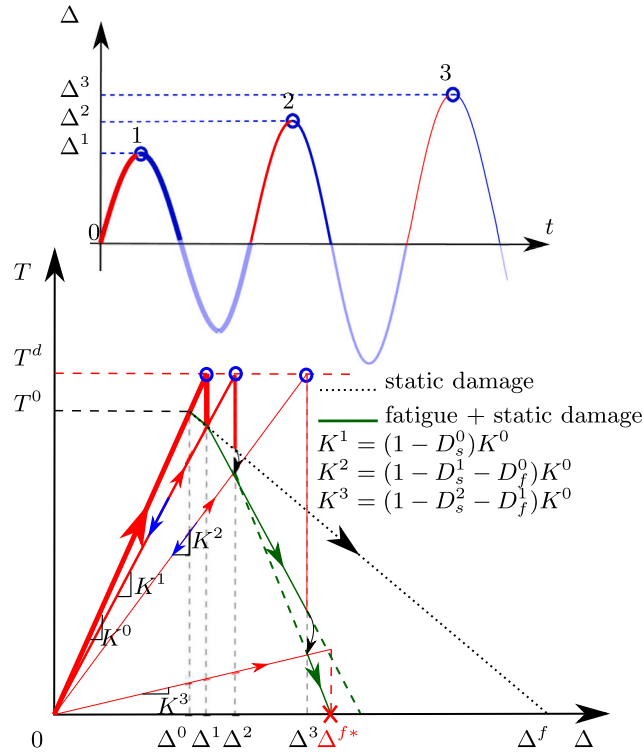


Fig. 10. Additive fatigue approach applied to a cohesive element at controlled load, T^d .

reach of the second peak, D_s^0 is replaced by D_s^1 . Once a first cycle elapsed, D_f ramps up from 0 to D_f^0 . Accordingly, the adhesive stiffness changes to $K^0(1 - D_s^1 - D_f^0)$. Importantly, D_f^0 deviates the slope of the initial static damage law so as to affect the computation of D_s^2 . The successive changes of this slope transform Δ^f into Δ^{f*} , referred to as effective relative displacement at failure.

3.3. On the implementation of an additive fatigue scheme

The static (interface opening) and fatigue damages evolve conjointly during cycling. For this reason, the additive scheme makes more sense than the non-additive scheme. Moreover, an additive scheme is unique compared to several non-additive variants. In practice, an additive scheme consists in degrading the adhesive stiffness based on $D_t = D_s + D_f$ where D_s , is evaluated following Demoura's implementation, and D_f incremented each ΔN cycles by $\epsilon_p^{-1/b}/C$ with ϵ_p amplitude of the maximum principal strain at a given adhesive point and C and b coefficients of Basquin's law. Flowchart 11 provides more insight into the additive fatigue scheme.

The implemented solution is as follows:

- (0) At the initial time increment $i = 0$, all damage variables are assigned to zero.

The following steps are processed in a loop while i is lower than or equal to N , the number of time steps specified by the user.

- (1) At each time increment $i > 0$, compute the current static damage D_s^i based, inter alia, on Δ_j^{i-1} with $j = n, s, t$ and D_s^{i-1} recovered from the state variables of the UEL subroutine.
- (2) Compute D_s^i and check the current status of the material (intact, damaged, failed). The adhesive cannot heal so $D_s^i > D_s^{i-1}$. D_s^i is assigned to 1, indicative of static failure, when $D_s^i \geq 1$.
- (3) Otherwise (no static failure), D_f^i has to be determined. If the current cycle, n , is not elapsed D_f^{n-1} is retained, otherwise, D_f^i takes D_f^n computed by Miner's fatigue damage accumulation. The Fortran code incorporates a Rainflow algorithm to extract cycles' peaks, required for the evaluation of fatigue damage increment. To speed up computations, the fatigue damage is accumulated over ΔN cycles, referred to as cycle-jump. Setting ΔN to 50 cycles resulted in a stable adhesive opening for both FE models of the uniaxial and biaxial assemblies. If $\Delta^{(f,i)} < 1$, the adhesive stiffness is degraded. Otherwise, the interface node is assumed fully damaged.
- (4) For the sake of simplicity, the degradation imputed to fatigue is supposed to affect all fracture modes identically.
- (5) The updated stiffness K^i permits the computation of displacement components Δ_j^i at the current increment. Δ_j^i variables are saved for the next iteration.

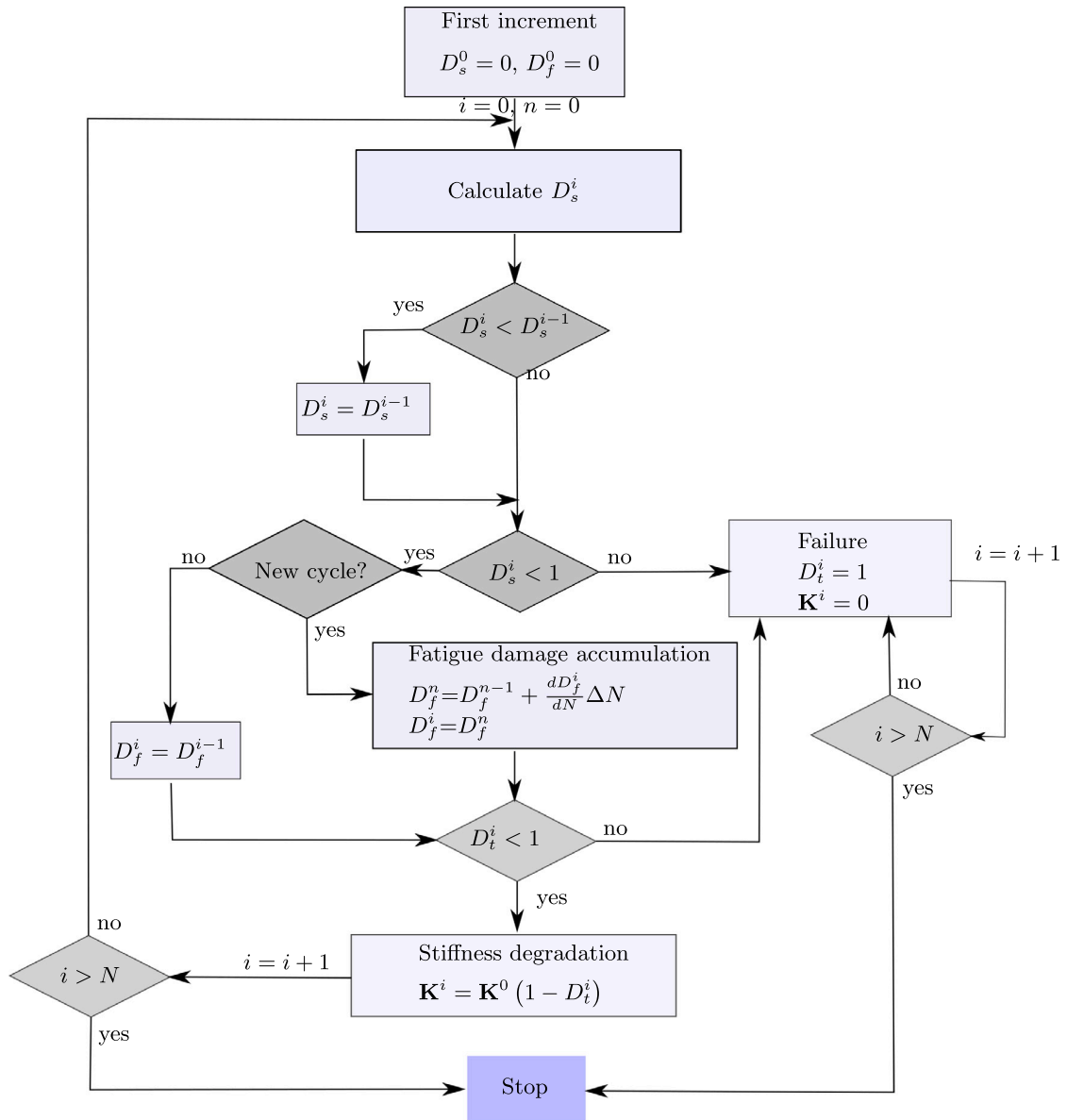


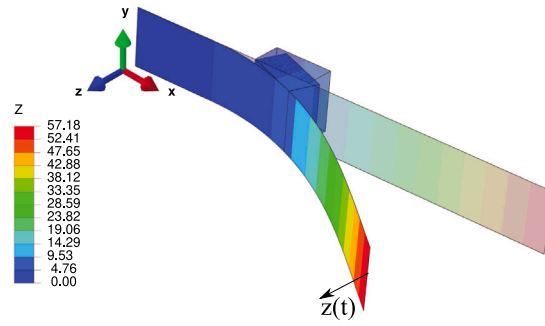
Fig. 11. Flowchart of the numerical fatigue simulation using an additive (static+fatigue) damage scheme.

3.4. Description of finite element models

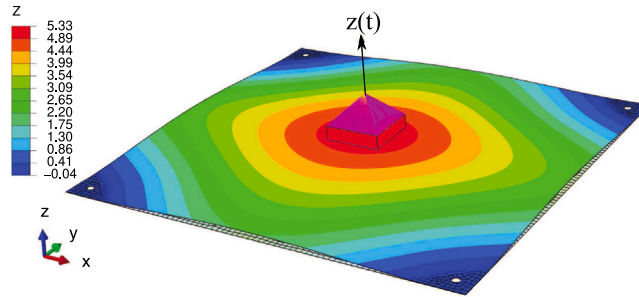
The uniaxial and biaxial models, illustrated in Fig. 12, were built under Abaqus software. S4 shell elements meshed the support as recommended in Ref. [33]. The ceramic component was meshed by Abaqus C3D8 brick elements. The adhesive layer was modelled by eight-node zero-thickness cohesive elements, created through a Fortran user element library (UEL) subroutine using the additive damage scheme outlined previously. The creation of cohesive elements from adjacent nodes of the support and the component drastically reduced the global size of models and avoided using tie/contact connectors. E , ν , and ρ designate Young's modulus, Poisson's ratio, and density of a given material, respectively. Table 3 reports the mechanical properties attributed to the adhesive and the substrates. The UEL subroutine was coupled with Abaqus Standard solver when running FE simulations. The fatigue loading consists in the imposition of an oscillatory deflection expressed by

$$z(t) = Z \sin(2\pi f t) \quad (10)$$

The excitation frequency, f , was set to 50 Hz as an average across resonance frequencies of the uniaxial and biaxial assemblies, and the time increment to 0.002 s. The application of a 'no-stop' option and the control of displacement helped simulations to



(a) Uniaxial bending adhesive assembly.



(b) Biaxial bending adhesive assembly.

Fig. 12. FE models of adhesive test assemblies.**Table 3**

Materials' mechanical properties [13,34].

Material	E MPa	ν	ρ kg/m ³	G_{nc} N/mm	G_{sc} N/mm	$T_s^0 = T_n^0$ MPa
Ablestik 8-2	3500	0.45	2300	0.15	1.50	25
E-glass	$E_l = 20,722$ $E_c = 18,750$ $G_{lc} = 6260$ $G_{lz} = G_{cz} = 5343$	0.158	1921			
Alumina	310,000	0.15	3940			

converge. According to Tomar et al. [35], the size of cohesive elements should meet two conditions to ensure convergence and mesh independence of the adhesive stress. First, the authors pointed out that the increase of the density of cohesive elements increases the overall deformation at constant applied load and finite initial stiffness of these elements. This increase/decrease of compliance/stiffness should not be excessive at the expense of computations' convergence. Therefore, the element size should be limited by a lower bound, e_l^{min} , defined by:

$$e_l^{min} = \frac{2\Delta_m^0 G_{tc} E_a (\sqrt{2} + 1)}{(T_n^0 T_s^0) (1 - \nu_a^2) (1 - \nu_a)} \quad (11)$$

Δ_m^0 depends on β mixed-mode ratio which is variable under mixed-mode conditions (refer to Appendix A). e_l^{min} was estimated at 0.0348 mm by considering $\min(\Delta_m^0)$ obtained at $\beta = 0$ corresponding to normal opening. Second, to accurately resolve the stress distribution, i.e., ensure stress mesh-size independence, the element size should be smaller than e_l^{max} referred to as cohesive zone size, defined by:

$$e_l^{max} = \frac{9\pi E_a G_{nc}}{32 (1 - \nu_a^2) (T_n^0)^2} \quad (12)$$

Using Ablestik 8-2 material properties, e_l^{max} was evaluated at 0.92 mm. This second condition was claimed by Alvarez et al. [36], who considered e_l larger than 2 mm problematic for the stability of the solution.

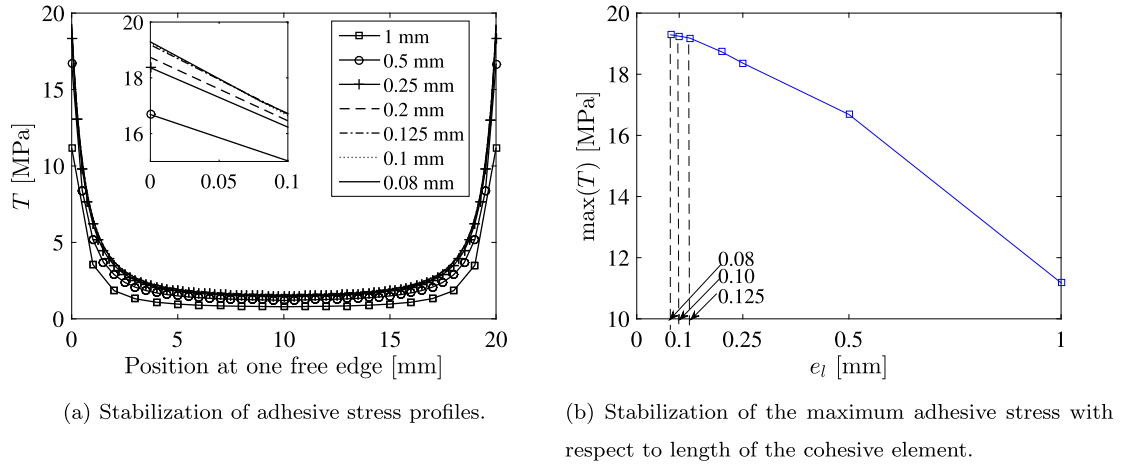


Fig. 13. Stabilization of adhesive stress with respect to the length of cohesive elements.

To convince of e_l bounds seen above, it was decided to follow the equivalent cohesive stress $T = \sqrt{\langle T_n \rangle^2 + T_s^2 + T_t^2}$ with respect to e_l . As viewed in Fig. 13a, stress profiles become invariant from $e_l = 0.25$ mm. This finding is better visualized in Fig. 13b reporting the evolution of $\max(T)$ with respect to e_l . Stress results are provided by simulation of the biaxial assembly at $Z = 0.5$ mm, intentionally chosen to avoid static adhesive damage. It was not bearable to run computations with e_l finer than 0.08 mm. Nevertheless, the decreasing slope of $\max(T)$ - e_l curve until the formation of a plateau corroborates the stabilization of the maximum stress. Given the above, $e_l = 0.25$ mm was considered effective since the 4.57% deviation of $\max(T)$ with report to $e_l = 0.1$ mm. This element size falls with the dimension of cohesive elements used by Chen et al. [37] for the simulation of a mixed-mode bending (MMB) specimen.

4. Derivation of a high cycle fatigue damage law

4.1. Derivation of a preliminary fatigue damage law

The initiation of adhesive failure in the uniaxial arrangement is assumed to coincide with the first failure of a node of the adhesive interface. Under this assumption, the $N_i - Z$ curve turns to be characteristic of the adhesive material. However, for generality, it is required to recast $N_i - Z$ in terms of a local metric that is sensitive to the internal strain state of the adhesive material. In the literature, the maximum principal strain of the adhesive denoted by ϵ_p makes unanimity. According to Khoramshad et al. [27], ϵ_p reads:

$$\epsilon_p = \frac{\langle \epsilon_n \rangle}{2} + \sqrt{\left(\frac{\langle \epsilon_n \rangle}{2}\right)^2 + \left(\frac{\epsilon_s}{2}\right)^2} \quad (13)$$

ϵ_n and ϵ_s refer to the normal and equivalent shear adhesive strains, respectively, according to

$$\epsilon_{n,s} = \frac{A_{n,s}}{h_a} \quad (14)$$

Not defined yet, Δ_s , refers to as equivalent shear displacement jump according to $\Delta_s = \sqrt{\Delta_s^2 + \Delta_t^2}$. h_a designates the thickness of the adhesive joint.

The uniaxial model was simulated at Z values of the uniaxial bending campaign. Fig. 14 maps the static damage at $Z = 8$ mm. A critical point, i.e., exhibiting the highest maximum principal strain, was spotted in the middle of the adhesive edge nearest to the clamped side of the E-glass plate, whatever Z . The failure of this point is assumed to trigger the adhesive joint failure. Under this assumption, the global Basquin's law $N_i - Z$ can be transformed into a local $N_i - \epsilon_p$ law, as shown in Fig. 15. The goodness of fit of the simulated data is worth 80% in terms of R-squared. Still, ϵ_p values are associated with uneven D_s . For the sake of generality, (N_i, ϵ_p) should refer to identical D_s , which is infeasible. Otherwise, the idea of this work consists in generating a preliminary $N - \epsilon_p$ fatigue law decoupled of the static damage according to $N = N_i / (1 - D_s)$. Fig. 15 shows that Basquin's law badly fits the simulated (N, ϵ_p) points (coloured in red). Indeed, assuming D_s constant under fatigue cycling is questionable. The increase of fatigue damage over cycles alters the interface opening causing ϵ_p to vary, which drives the need to calibrate Basquin's parameters, C and b . Bear in mind that the fatigue damage law is valid as long as D_s is within 1. This limit corresponds to $Z = 18$ mm, or 65,140 $\mu\epsilon$, in the aforementioned critical point of the uniaxial model.

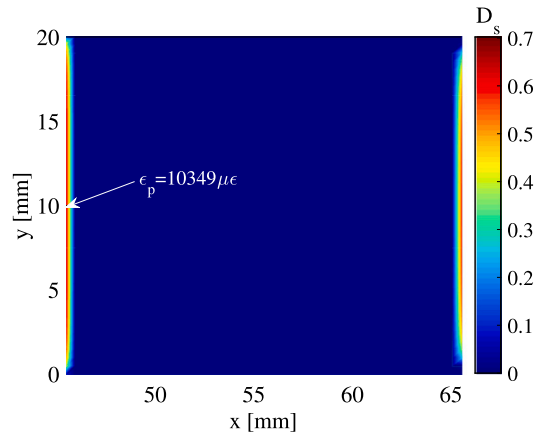


Fig. 14. Map of static damage: $20 \times 20 \text{ mm}^2$ adhesive joint under maximum allowed support deflection $Z = 8 \text{ mm}$.

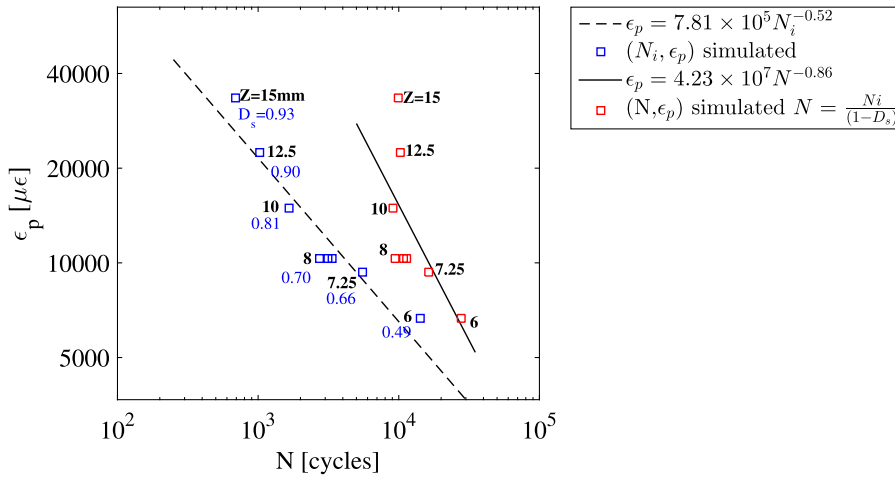


Fig. 15. Generation of the preliminary fatigue damage law $\epsilon_p - N$ of Ablestik 8-2 adhesive.

4.2. Calibration of the fatigue damage law

Graner Solana et al. [38] determined b directly from stress-life curves obtained experimentally by standard single lap joint shear tests under controlled loads, then calibrated C by a trial and error method. Here, the same paradigm is generalized to the two parameters of $N - \epsilon_p$ law. So far, C and b were initially estimated at 4.23×10^7 and -0.86 , as indicated in Fig. 15. Rather than simulating all tested deflections in [6–15] mm range, it was more bearable in terms of CPU time cost to calibrate the preliminary fatigue law at 7.25 mm and 12.5 mm Z levels. Few attempts permitted to update C and b at 15.42×10^6 and -0.7 , respectively. The validation of the calibrated fatigue law at $Z = 10 \text{ mm}$, not used for calibration, resulted in a 9.90% relative error between the simulated and experimental N_i . Fig. 16, reporting the plot of the updated $N - \epsilon_p$ law and all simulated (N, ϵ_p) , brings more evidence on the acceptable goodness of fit through Basquin's law, which to retain it. Red crosses shown in Fig. 16 indicate ϵ_p^1 and $\epsilon_p^{N_i}$ referring to as ϵ_p levels at the first loaded cycle and after N_i loaded cycles. Beyond the calibration of $\epsilon_p - N$, other interesting findings could be drawn from fatigue simulations at $Z = (7.25, 10, 12.5) \text{ mm}$. Fig. 17 depicts D_i evolutions with respect to N at four points picked at borders of the adhesive joint. These evolutions led to the detection of N_i at $D_i = 1$. Simulated results are identical from the two sides of the x -axis of symmetry of the uniaxial model. Fig. 18 illustrates the interplay between damage variables D_s , D_f , and D_t during cycling. As surmised previously, D_s varies during fatigue cycling. The lower Z , the more pronounced is the variation of D_s and ϵ_p over cycles, as shown in Figs. 19 and 17. Let (D_s^1, ϵ_p^1) and $(D_s^{N_i}, \epsilon_p^{N_i})$ stand for (D_s, ϵ_p) values at the first loaded cycle and at the initiation of specimen's debonding, respectively. The decrease of the adhesive stiffness under fatigue does not necessarily imply an increase in the adhesive strain. Fig. 20 shows a zoom on the evolution of ϵ_p at the critical middle left point reporting all the simulated values over the ramping up phase followed by peak values extracted at each ΔN , which build the envelope of ϵ_p . Fig. 19 reports opposite trends of ϵ_p versus N for points in left and right bond-lines. So, the geometry of the test specimen plays a role in the distribution of the adhesive strain, which should warn against hasty interpretations emanating from the experimental

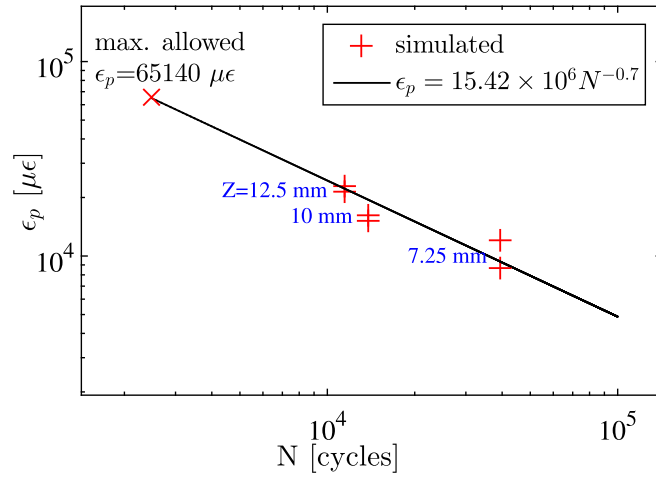


Fig. 16. Calibrated $\epsilon_p - N$ fatigue law of Ablestik 8-2 adhesive.

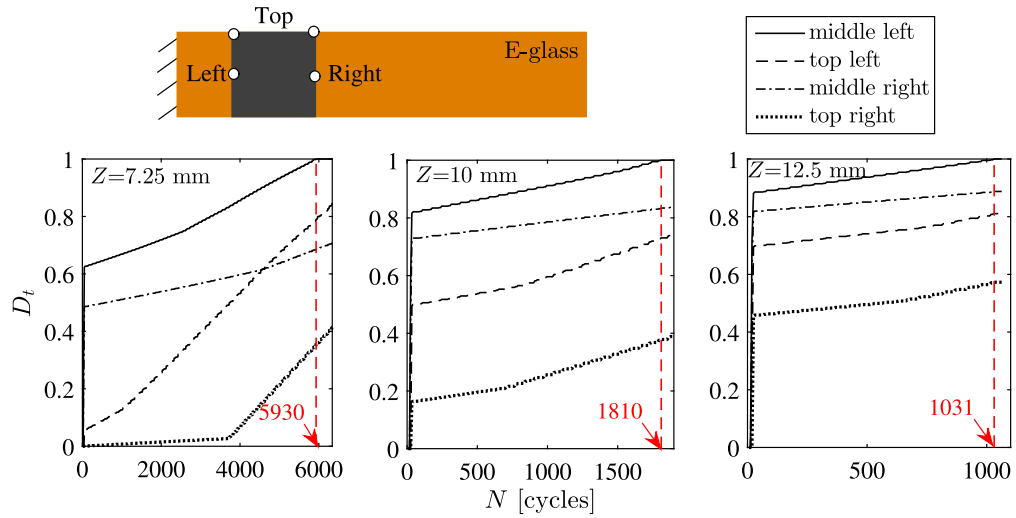


Fig. 17. Evolution of the total damage in different material points of the adhesive upon cyclic uniaxial bending.

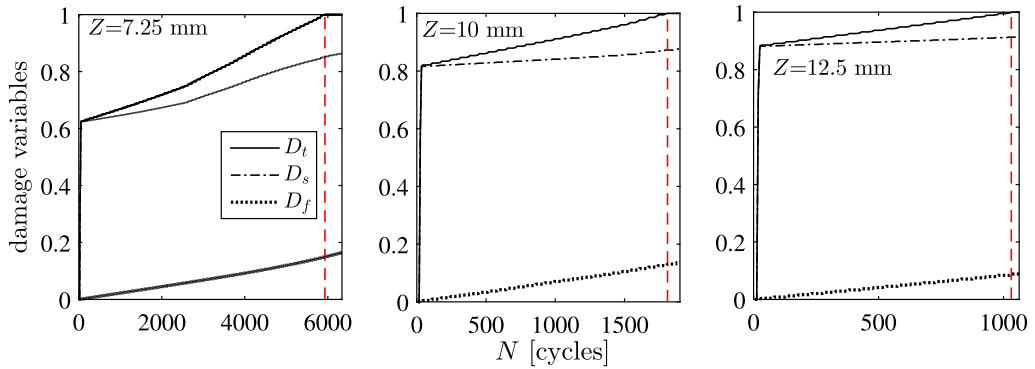


Fig. 18. Evolution of damage variables in different adhesive points upon cyclic uniaxial bending.

recording of the adhesive strain. Table 4 summarizes the principal simulated results on the uniaxial model with their comparison to experiments.

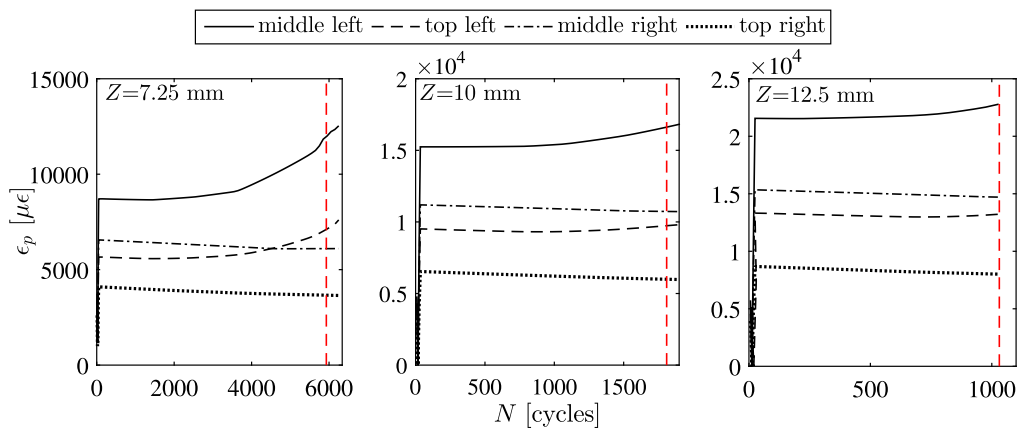


Fig. 19. Evolution of the maximum principal strain in different adhesive points upon cyclic uniaxial bending.

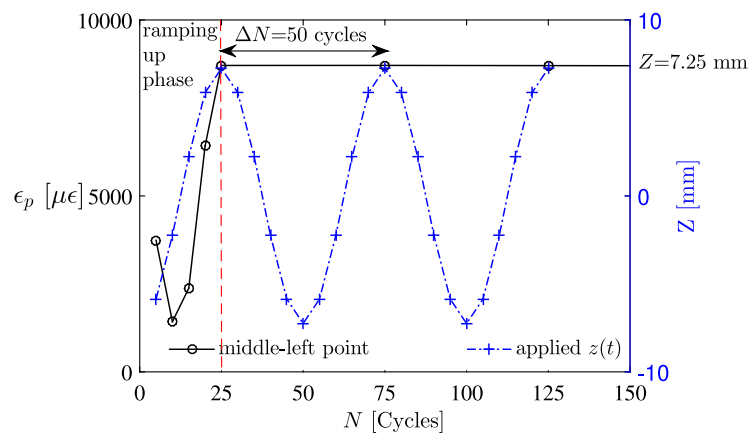


Fig. 20. Zoom on the evolution of the maximum principal strain in the small N .

Table 4

Summary of simulated results under uniaxial bending.

Z [mm]	N_i	$N_i(\text{exp})$	$\delta(N_i)$	N	D_s^1	$D_s^{N_i}$	D_f	ϵ_p^1	$\epsilon_p^{N_i}$
7.25	5930	5514	7.54%	40,067	0.662	0.853	0.148	8708	12,002
10	1810	1647	9.90%	13,816	0.816	0.873	0.131	15,243	16,604
12.5	1031	1023	0.78%	11,647	0.881	0.913	0.088	21,558	22,773

5. Validation of the synthesized fatigue damage law

Fatigue simulations were carried out on the biaxial assembly for $Z = 1.5$ and 3 mm to examine the relevance of the calibrated $N - \epsilon_p$ law. Fig. 21 reports D_i and ϵ_p evolutions for $Z = 3$ mm. Obtaining identical results at the four corners and four edges' middles testifies the good execution of fatigue computations. Qualitatively, tracking the percentile of the opened adhesive joint asserted the smooth propagation of interface opening. This is obvious from plots of this indicator for $Z = 1.5$ mm and $Z = 3$ mm in Figs. 22 and 23, respectively. Quantitatively, the simulated N_f of 3722 cycles for $Z = 3$ mm and 331,300 cycles for $Z = 1.5$ mm do not exactly agree with their respective experimental counterparts detected at 2350 and 650,367 cycles. Despite this discrepancy, it is promising the fact that $N_f = 331,300$ cycles is in between 34,877 and 650,367 standing for the experimental N_f values for $Z = 2$ mm and $Z = 1.5$ mm. Similarly, $N_f = 3722$ is located between 12,575 and 2336 being the experimental N_f values for $Z = 2.5$ mm and $Z = 3$ mm. Therefore, the numerical prediction in biaxial bending resulted in a meaningful order of magnitude of N_f .

Fatigue simulations are afflicted with numerous factors. Here are a few highlights:

- Developing a holistic prediction model that incorporates both nucleation and propagation laws is intricate. More complexity stems, according to Quaresimin and Ricotta [39], from the dependence of the proportion of initiation cycles to propagation cycles on the overlap length and stress levels. For Scotch-Weld 9323 B/A epoxy adhesive, the crack initiation ranges between

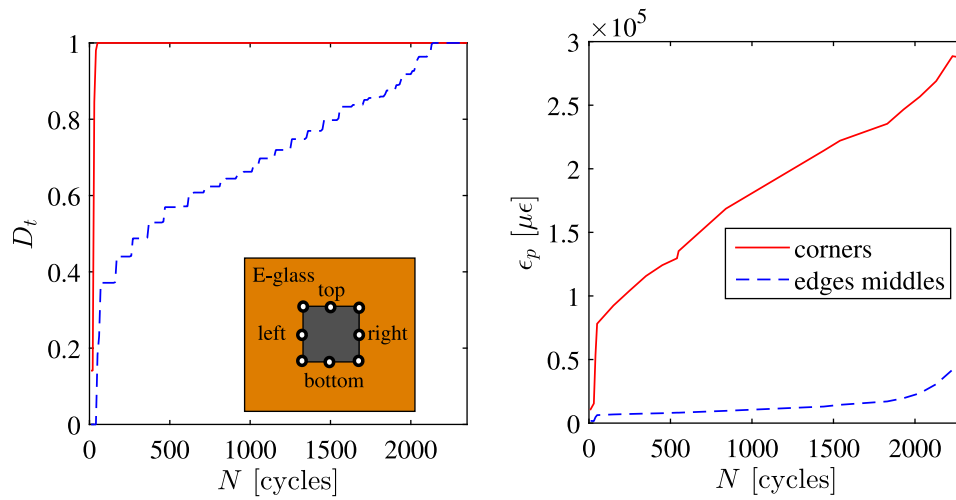


Fig. 21. Verification of the initiation of failure in points at borders of the adhesive joint in the biaxial configuration at $Z = 3$ mm.

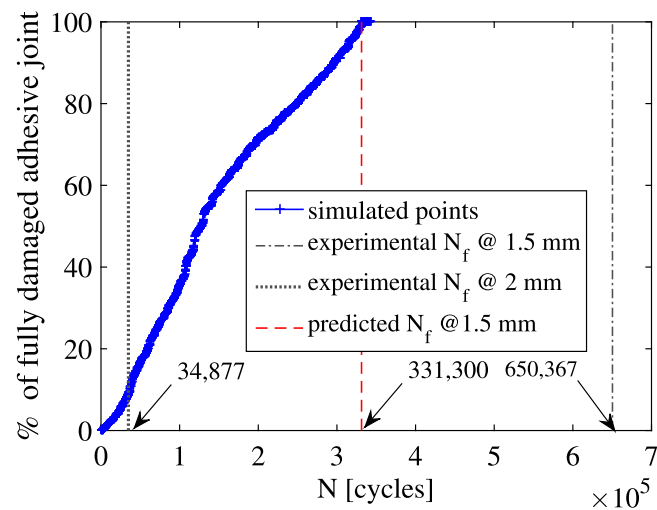


Fig. 22. Prediction of total fatigue failure (rupture) at $Z = 1.5$ mm in biaxial configuration.

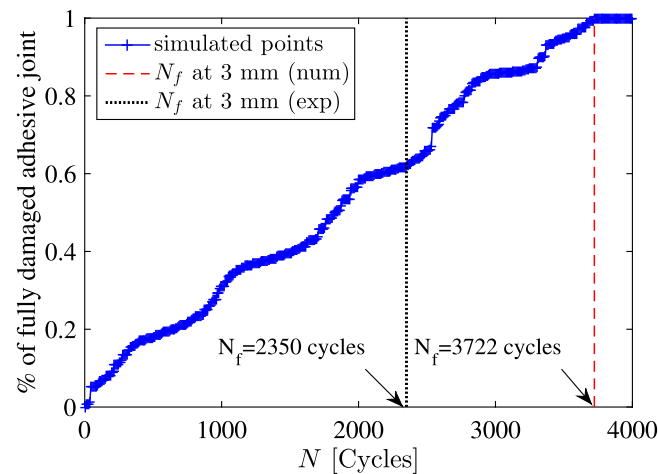


Fig. 23. Prediction of total fatigue failure (rupture) at $Z = 3$ mm in biaxial configuration.

20% to more than 70% of the adhesive lifetime, which is a wide interval [39]. Furthermore, a prediction model cannot be generalized to all the adhesives. Although, Scotch-Weld 9323 adhesive compares to Ablestik 8–2, in terms of its 2.87 GPa Young's modulus and 0.37 Poisson's ratio, the failure of Ablestik 8–2 starts from the first cycles, not from 20% of its lifetime.

- The choice of the power propagation law constrains the mechanism of adhesive opening under mixed-mode conditions in a way that can be unrealistic.
- It is substantial to take the dynamic behaviour of the adhesive into account. For instance, the higher structural damping, the more the fatigue life of the adhesive increases. Besides, cohesive properties at 50 Hz, as simulated here, or at 300 Hz on real electronic boards, may differ from ones emanating from static tests.

6. Conclusions

The present work unveils novel fatigue test assemblies made of a rigid ceramic component adhesively bonded to flexible E-glass support. The fatigue test of Ablestik 8–2 epoxy adhesive under uniaxial and biaxial bending of the E-glass support yielded cycles to the initiation and total failure of the adhesive joint, respectively. Uniaxial and biaxial bending test data, i.e., deflection versus fatigue cycles, were fitted using two distinct Basquin's laws. A numerical effort focused on recasting the deflection-based fatigue law obtained under uniaxial bending into an intrinsic fatigue law of the adhesive. The idea of this work consists in keeping the Basquin's form while substituting the deflection with the maximum principal strain in each adhesive point. The dependence of the strain metric on the local static damage obliged the calibration of the coefficients of the strain-based fatigue damage law through the correlation, at two different deflection levels, between simulated and measured cycles to failure initiation. Simulations with the resulting fatigue law yielded a satisfactory prediction of the initiation of failure under uniaxial bending while ensured a consistent order of prediction of the fatigue lifetime of the adhesive joint under biaxial bending. This work elaborated guidelines regarding the choice of size for cohesive elements for the sake of ensuring the convergence and accuracy of simulations, also as concerns the implementation of an additive damage computation scheme that combines static and fatigue damage models.

Still, there is a lot of room for improvement. First, the calibration of the fatigue damage law can be improved by involving more data points. Second, testing additional uniaxial assemblies could establish statistics on Basquin's law parameters. Third, testing additional biaxial assemblies is required to assess the accuracy of the prediction made from the additive scheme. Fourth, the detection of the initiation of failure under biaxial bending could ascertain the applicability of the strain-based fatigue law to this arrangement, figure out the proportion between crack initiation and propagation over the total fatigue lifetime, and examine the dependency of this proportion on the applied load. Eventually, tracking the crack propagation with enhanced instrumentation would decide whether to retain the current crack propagation model or look at other models.

Declaration of competing interest

The authors declare that they have no known competing financial interests or personal relationships that could have appeared to influence the work reported in this paper.

Appendix A. Cohesive zone modelling approach

The cohesive zone modelling stipulates that the adhesive interface opens in normal, scissoring shear, and transverse shear modes producing Δ_n , Δ_s , Δ_t , relative displacements between separated substrates, respectively, called also displacement jumps. In this framework, a traction-separation law is commonly deployed to model the mechanical behaviour of the adhesive interface. This law establishes the relationship between unknown cohesive traction components, T_i , having a unit of stress, and known Δ_i with $i = n, s, t$. Common cohesive laws are described by triangular (bilinear), exponential, trapezoidal, rectangular shapes [40], depending on the ductility of the adhesive. Alfano [41] argued that the trapezoidal law conducts to worst approximation and generates high oscillations during the material softening. Conversely, according to Fernandes and Campilho [42], the bilinear law offers an overall acceptable fit for common adhesives and provides the best trade-off between computation cost and accuracy of prediction. Therefore, this work relies on a bilinear law that reads:

$$T_i = (1 - D_s) K_i \Delta_j - D_s K_i \delta_{ni} \langle -\Delta_n \rangle \quad i, j = n, s, t \quad (\text{A.1})$$

K_i are terms of the undamaged secant stiffness tensor, \mathbf{K} , defined by

$$\mathbf{K} = \begin{bmatrix} K_s & 0 & 0 \\ 0 & K_s & 0 \\ 0 & 0 & K_n \end{bmatrix} \quad (\text{A.2})$$

K_s and K_n represent shear and normal stiffness terms, respectively. It is of great importance regarding the prediction of the elastic response of the adhesive to express the former stiffness terms with respect to mechanical and geometric parameters of the adhesive joint as follows

$$K_n = \frac{E_a^e}{h_a} \quad K_s = \frac{G_a}{h_a} \quad \text{with} \quad E_a^e = \frac{E_a (1 - \nu_a)}{1 - \nu_a - 2\nu_a^2} \quad (\text{A.3})$$

E_a , ν_a , G_a , h_a are Young's modulus, Poisson ratio, shear modulus and thickness of the adhesive, respectively. The off-diagonal stiffness terms can be set to zero since that the evolves in a pre-definite direction [43] as concerns the uniaxial and biaxial adhesive assemblies. In case of more than one opening mode, the contribution of each mode is traditionally evaluated through β_s and β_t , mixed-mode ratios defined as follows

$$\beta_{s,t} = \frac{\Delta_{s,t}}{\Delta_n} \quad \text{if } \Delta_n > 0 \quad (\text{A.4})$$

To obtain shorter equations, β_s and β_t are, when possible, merged into a unique mixed-mode ratio denoted by

$$\beta = (\beta_s^2 + \beta_t^2)^{\frac{1}{2}} \quad (\text{A.5})$$

The quadratic nominal stress criterion is deemed as a damage initiation criterion, which is expressed by

$$\left(\frac{\langle T_n \rangle}{T_n^0} \right)^2 + \left(\frac{T_s}{T_s^0} \right)^2 + \left(\frac{T_t}{T_t^0} \right)^2 = 1 \quad (\text{A.6})$$

Knowing that $T_i = K_i \Delta_i$ and by merging Eqs. (A.4) and (A.5) into Eq. (A.6), the expression of the equivalent mixed-mode displacement jump at damage initiation, Δ_m^0 , comes out as follows

$$\Delta_m^0 = \Delta_s^0 \Delta_t^0 \Delta_n^0 \left[\frac{1 + \beta^2}{(\Delta_s^0 \Delta_t^0)^2 + (\beta_s \Delta_n^0 \Delta_t^0)^2 + (\beta_t \Delta_n^0 \Delta_s^0)^2} \right]^{\frac{1}{2}} \quad (\text{A.7})$$

Under the assumptions of T_s^0 and T_t^0 equal, and K_s and K_t equal, Eq. (A.7) can be rewritten as follows

$$\Delta_m^0 = \Delta_n^0 \Delta_s^0 \left[\frac{1 + \beta^2}{\Delta_s^{02} + \beta^2 \Delta_n^{02}} \right]^{\frac{1}{2}} \quad (\text{A.8})$$

The total energy release rate under mixed-mode conditions, G_T , is defined by the following sum

$$G_T = G_n + G_s + G_t = \frac{1}{2} K_n \Delta_{nm}^0 \Delta_{nm}^f + \frac{1}{2} K_s \Delta_{sm}^0 \Delta_{sm}^f + \frac{1}{2} K_t \Delta_{tm}^0 \Delta_{tm}^f \quad (\text{A.9})$$

The terms G_i represent individual mixed-mode energy release rates expressed by

$$G_i = \frac{1}{2} K_i \Delta_{im}^0 \Delta_{im}^f \quad (\text{A.10})$$

Δ_{im}^0 and Δ_{im}^f are i th mixed-mode displacement jumps of individual mode at damage onset and failure, respectively. In contrast to single-mode terms, the latter are given by

$$\Delta_{sm}^{0,f} = \frac{\beta_s \Delta_m^{0,f}}{\sqrt{1 + \beta^2}} \quad \Delta_{tm}^{0,f} = \frac{\beta_t \Delta_m^{0,f}}{\sqrt{1 + \beta^2}} \quad \Delta_{nm}^{0,f} = \frac{\Delta_m^{0,f}}{\sqrt{1 + \beta^2}} \quad (\text{A.11})$$

A damage propagation criterion or fracture model provides G_{mc} , which is at the prediction of total failure corresponding to $G_T = G_{mc}$. Alternatively, G_{mc} could be expressed by

$$G_{mc} = \frac{1}{2} K_m \Delta_m^0 \Delta_m^f \quad (\text{A.12})$$

K_m is the mixed-mode stiffness of the material that is obtained by substituting Eqs. (A.11) into Eq. (A.10) then by equating the resulting G_T to G_{mc} which makes $\Delta_m^0 \Delta_m^f$ drop and leads to the following form

$$K_m = \frac{K_n + \beta^2 K_s}{1 + \beta^2} \quad (\text{A.13})$$

The equivalence between G_T and G_{mc} permits to extract the mixed-mode displacement jump at damage onset, Δ_m^f , as follows

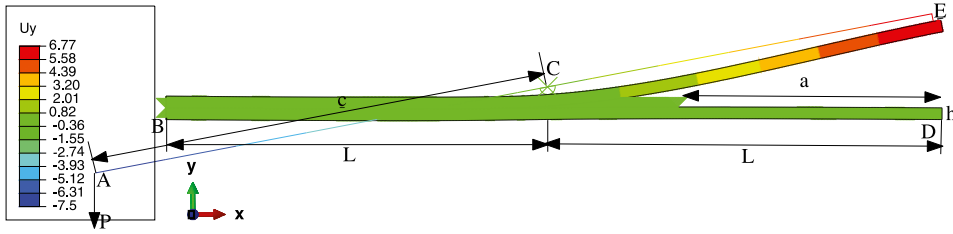
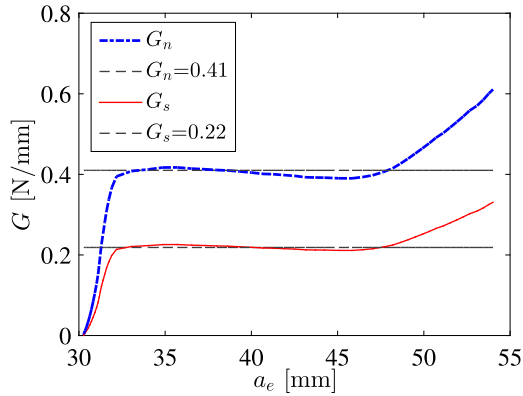
$$\Delta_m^f = \frac{2(G_T = G_{mc})}{K_m \Delta_m^0} \quad (\text{A.14})$$

The power law belongs to the class of non-interaction fracture criteria. This law is expressed as follows:

$$\left(\frac{G_n}{G_{nc}} \right)^\gamma + \left(\frac{G_s}{G_{sc}} \right)^\gamma + \left(\frac{G_t}{G_{tc}} \right)^\gamma = 1 \quad (\text{A.15})$$

A linear fracture energetic criterion is considered in this work, which corresponds to $\gamma = 1$. According to Eq. (A.14), knowing G_{mc} is required to obtain Δ_m^f . The expression of G_i in function of Δ_m^0 and Δ_m^f through relations (A.11) permits to express G_{mc} as follows

$$G_{mc} = (K_n + \beta^2 K_s) \left[\frac{K_n}{G_{nc}} + \frac{\beta_s^2 K_s}{G_{sc}} + \frac{\beta_t^2 K_s}{G_{tc}} \right]^{-1} \quad (\text{A.16})$$

Fig. B.24. MMB specimen ($L = 51$ mm, $a = 35$ mm, $h = 1.56$ mm, $c = 60$ mm).

(a) R-curves of fracture energy components

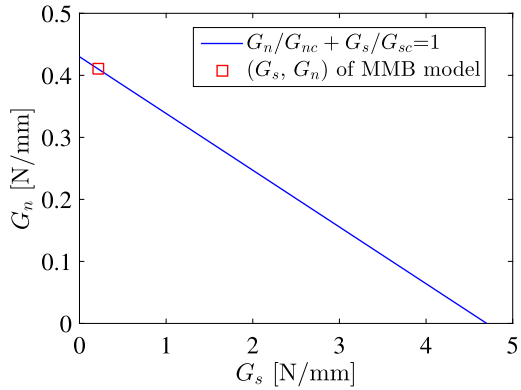
(b) Fracture energies in $G_n - G_s$ space for $G_{nc}=0.43$ N/mm, $G_{sc}=4.7$ N/mm and $T_n^0 = T_s^0 = 23$ MPa

Fig. B.25. Validation of Demoura's variant of Camanho's damage model on a standard MMB prototype.

Appendix B. Validation of the user element subroutine of De Moura's implementation of Camanho's damage model

This appendix deals with the validation of De Moura's variant of Camanho's damage model on a standard MMB specimen, as did De Moura et al. [30] for the validation of their proposal. The MMB specimen offers the advantage of holding the global mixed-mode ratio constant following

$$\frac{G_n}{G_s} = \frac{4}{3} \left(\frac{3c - L}{c + L} \right)^2 \quad (\text{B.1})$$

For brevity, only results generated for a linear power law with utmost general cohesive properties are considered. Fig. B.24 illustrates the chosen MMB specimen of h out-of-plane thickness set to 25 mm (not presented). The top and bottom substrates were meshed with 0.1×0.1 mm² plane stress four-node CS4P elements of Abaqus. The interface between the substrates is open along a distance while its remaining part contains zero-thickness adhesive elements. The cohesive model under investigation is assigned to these elements. The assembly is clamped from its end points B and D of the bottom substrate. The second end E and the intermediate point C are tied against end of the top substrate and a rigid cylinder that comes in contact with the top substrate, respectively. A displacement was applied along y -axis to the point A, part of the rigid arm [AE]. G_n is provided by

$$G_n = \frac{12P_n^2}{B^2h} \left(\frac{a_{ne}^2}{Eh^2} + \frac{1}{5G} \right) \quad (\text{B.2})$$

a_{ne} is mode-I equivalent crack length expressed in terms of C_n compliance of loading mode-I as follows

$$C_n = \frac{A_n}{P_n} = \frac{8a_{ne}^3}{Ebh^3} + \frac{12a_{ne}}{5GBh} \quad (\text{B.3})$$

G_s is provided by

$$G_s = \frac{9P_s^2 a_{se}^2}{16B^2 E h^3} \quad (\text{B.4})$$

a_{se} is mode-II equivalent crack length expressed in terms of C_s compliance of loading mode-II as follows

$$C_s = \frac{A_s}{P_s} = \frac{3a_{se}^3 + 2L^3}{8EBh^3} + \frac{3L}{10GBh} \quad (\text{B.5})$$

The applied loads P_n and P_s are defined as follows:

$$P_n = \frac{3c - L}{4L} P \quad P_s = \frac{c + L}{L} P \quad (\text{B.6})$$

The displacement of E corresponds to mode-I displacement jump denoted by Δ_n . Mode-II displacement denoted by Δ_s is worth $\Delta_C + \Delta_n/4$ with Δ_C displacement of C. Δ_C and Δ_n obtained numerically permit to evaluate Δ_{ne} and Δ_{se} according to Eqs. (B.2) and (B.4).

As a result, Fig. B.25a shows the evolution of $G_{n,s}$ in function of $\Delta_{ne,se}$, referred to as R-curves. Of interest are $G_{n,s}$ values in the plateau region which refer to a self-similar crack growth [30]. Their ratio G_n/G_s is evaluated at 1.86 that is roughly equal to 1.81 obtained from the characteristic equation (B.1). This upshot validates the relevance of the implementation of De Moura's variant. Furthermore, Fig. B.25b shows a perfect agreement between (G_s , G_n) obtained on R-curves and the analytical $G_s - G_n$ evolution of the linear power law. This puts evidence in the physical consistency of DeMoura's implementation at a global scale and constant mixed-ratio. Previous validations made on actual adhesive assemblies were local (at nodes) and devoted for mixed-mode ratios.

References

- [1] Lagier R. Ariane 5 user's manual. Technical report, ArianeSpace Service and Solutions; 2016.
- [2] Timmins AR, Heuser RE. A study of first-day space malfunctions. Technical report, USA: Goddard Space Flight Center; 1970.
- [3] Ben Fekih L, Kouroussis G, Verlinden O. Verification of empirical warp-based design criteria of space electronic boards. *Microelectron Reliab* 2015;55(12):2786–92.
- [4] Steinberg DS. Vibration analysis for electronic equipment. John Wiley and Sons; 2000.
- [5] Gomatam RR, Sancaktar E. Effects of various adherend surface treatments on fatigue behavior of joints bonded with a silver-filled electronically conductive adhesive. *J Adhes Sci Technol* 2005;19(8):659–78.
- [6] Kinloch AJ, Osiyemi SO. Predicting the fatigue life of adhesively-bonded joints. *J Adhes* 1993;43(1–2):79–90.
- [7] Liu P, Huang J. The fatigue life analysis of conductive adhesive. In: 14th international conference on electronic packaging technology. 2013, p. 804–8.
- [8] Azari S, Papini M, Spelt JK. Effect of adhesive thickness on fatigue and fracture of toughened epoxy joints - part i: Experiments. *Eng Fract Mech* 2011;78(1):153–62.
- [9] Chiu TC, Lu W, Hua C-A. An experimental setup for characterizing subcritical debonding of materials interface under mixed mode fatigue loading. *Int J Fatigue* 2018;114:109–19.
- [10] Walter T, Khatibi G, Nelhiebel M, Stefenelli M. Characterization of cyclic delamination behavior of thin film multilayers. *Microelectron Reliab* 2018;88–90:721–5.
- [11] Guzek J, Azimi H, Suresh S. Fatigue crack propagation along polymer-metal interfaces in microelectronic packages. *IEEE Trans Compon Packag Manuf Technol Part A* 1997;20(4):496–504.
- [12] Jung S, Paik K. Effects of the adhesion strength on the bending fatigue behavior of cu pattern laminated fabrics using b-stage non-conductive films (ncfs). In: 2018 IEEE 68th electronic components and technology conference (ECTC). 2018, p. 2301–6.
- [13] Ben Fekih L, Verlinden O, De Fruytier Ch, Kouroussis G. Novel test prototype for the determination of mode-i fracture parameters: application to adhesively bonded electronics. *Procedia Struct Integr* 2017;5:5–12.
- [14] Bak BLV, Turon A, Lindgaard E, Lund E. A benchmark study of simulation methods for high-cycle fatigue-driven delamination based on cohesive zone models. *Compos Struct* 2017;164:198–206.
- [15] Kawashita LF, Hallett RS. A crack tip tracking algorithm for cohesive interface element analysis of fatigue delamination propagation in composite materials. *Int J Solids Struct* 2012;49(21):2898–913.
- [16] Bak BLV, Sarrado C, Turon A, Costa J. Delamination under fatigue loads in composite laminates: A review on the observed phenomenology and computational methods. *Appl Mech Rev* 2014;66(6).
- [17] Pironi A, Moroni F. Simulation of mixed-mode i/ii fatigue crack propagation in adhesive joints with a modified cohesive zone model. *J Adhes Sci Technol* 2011;25(18):2483–99.
- [18] Turon A, Costa J, Camanho PP, Dávila CG. Simulation of delamination in composites under high-cycle fatigue. *Composites A* 2007;38(11):2270–82.
- [19] Harper PW, Hallett SR. A fatigue degradation law for cohesive interface elements - development and application to composite materials. *Int J Fatigue* 2010;32(11):1774–87.
- [20] Kiefer K. Simulation of high-cycle fatigue-driven delamination in composites using a cohesive zone model (Ph.D. thesis), Imperial College London, Department of Aeronautics; 2014.
- [21] Peerlings RHJ, Brekelmans WAM, Borst, Rand de, Geers MGD. Gradient-enhanced damage modelling of high-cycle fatigue. *Internat J Numer Methods Engrg* 2000;49(12):1547–69.
- [22] Roe KL, Siegmund T. An irreversible cohesive zone model for interface fatigue crack growth simulation. *Eng Fract Mech* 2003;70(2):209–32.
- [23] Robinson P, Galvanetto U, Tumino D, Bellucci G, Violeau D. Numerical simulation of fatigue-driven delamination using interface elements. *Internat J Numer Methods Engrg* 2005;63(13):1824–48.
- [24] Bouvard JL, Chaboche JL, Feyel F, Gallerneau F. A cohesive zone model for fatigue and creep-fatigue crack growth in single crystal superalloys. *Int J Fatigue* 2009;31(5):868–79.
- [25] Bak BLV, Turon A, Lindgaard E, Lund E. A simulation method for high-cycle fatigue-driven delamination using a cohesive zone model. *Internat J Numer Methods Engrg* 2016;106(3):163–91.
- [26] Carreras L, Turon A, Bak BLV, Lindgaard E, Renart J, Martin de la Escalera F, Essa Y. A simulation method for fatigue-driven delamination in layered structures involving non-negligible fracture process zones and arbitrarily shaped crack fronts. *Composites A* 2019;122:107–19.
- [27] Khoramshad H, Crocombe AD, Kali K, Ashcroft I. Predicting fatigue damage in adhesively bonded joints using a cohesive zone model. *Int J Fatigue* 2010;32:1146–58.
- [28] Ben Fekih L, Kouroussis G, Verlinden O. Spectral-based fatigue assessment of ball grid arrays under aerospace vibratory environment. *Key Eng Mater* 2013;569–570:425–32.
- [29] Camanho P, Davila CG. Mixed-mode decohesion finite elements for the simulation of delamination in composite materials. Technical report, Hampton, USA: NASA Langley Research Center; 2002.
- [30] De Moura MFSF, Gonçalves JPM, Silva FGA. A new energy based mixed-mode cohesive zone model. *Int J Solids Struct* 2016;102–103:112–9.
- [31] Jimenez S, Duddu R. On the parametric sensitivity of cohesive zone models for high-cycle fatigue delamination of composites. *Int J Solids Struct* 2016;82:111–24.
- [32] Ghovanlou MK, Jahed H, Khajepour A. Cohesive one modeling of fatigue crack growth in brazed joints. *Eng Fract Mech* 2014;120:43–59.
- [33] Ben Fekih L, Verlinden O, Kouroussis G. Mechanical characterization of e-glass laminates under large bending. *Compos Struct* 2021;255.

- [34] Ben Fekih L, Verlinden O, Kouroussis G, DeFrutier Ch. On the non-linear dynamic properties of trabond 8.2 structural adhesive. In: ICSV 2016-23rd international congress on sound and vibration: from ancient to modern acoustics. 2016.
- [35] Tomar V, Zhai J, Zhou M. Bounds for element size in a variable stiffness cohesive finite element model. *Internat J Numer Methods Engrg* 2004;61(11):1894–920.
- [36] Alvarez D, Blackman BRK, Guild FJ, Kinloch AJ. Mode I fracture in adhesively-bonded joints: A mesh-size independent modelling approach using cohesive elements. *Eng Fract Mech* 2014;115:73–95.
- [37] Chen J, Crisfield M, Kinloch AJ, Busso EP, Matthews FL, Qiu Y. Predicting progressive delamination of composite material specimens via interface elements. *Mech Compos Mater Struct* 1999;6(4):301–17.
- [38] Graner Solana A, Crocombe AD, Ashcroft IA. Fatigue life and backface strain predictions in adhesively bonded joints. *Int J Adhes Adhes* 2010;30:36–42.
- [39] Quaresimin M, Ricotta M. Fatigue behaviour and damage evolution of single lap bonded joints in composite material. *Compos Sci Technol* 2006;66(2):176–87.
- [40] Dugdale DS. Yielding of steel sheets containing slits. *J Mech Phys Solids* 1960;8(2):100–4.
- [41] Alfano G. On the influence of the shape of the interface law on the application of cohesive-zone models. *Compos Sci Technol* 2006;66(6):723–30.
- [42] Fernandes RL, Campilho RDSG. Testing different cohesive law shapes to predict damage growth in bonded joints loaded in pure tension. *J Adhes* 2017;93(1–2):57–76.
- [43] Dimitri R, Trullo M, De Lorenzis L, Zavarise G. Coupled cohesive zone models for mixed-mode fracture: A comparative study. *Eng Fract Mech* 2015;148:145–79.